Acta Materialia 275 (2024) 120037

Contents lists available at ScienceDirect

Acta Materialia

journal homepage: www.elsevier.com/locate/actamat

Full length article

Understanding grain boundary segregation and solute drag using computational and machine learning studies

Malek Alkayyali [a], Milad Taghizadeh [b], Fadi Abdeljawad [a,b,*]

[a] Department of Mechanical Engineering, Clemson University, Clemson, SC, 29634, USA
[b] Department of Materials Science and Engineering, Lehigh University, Bethlehem, PA, 18015, USA

ARTICLE INFO

Keywords:
Grain boundaries
Solute segregation
Solute drag
Machine learning
Nanocrystalline alloys

ABSTRACT

Grain boundary (GB) solute segregation has been used as a strategy to tailor the properties and processing pathways of a wide range of metallic alloys. GB solute drag results when segregated alloying elements exert a resistive force on migrating GBs hindering their motion. While GB segregation has been the subject of active research, a detailed understanding of solute drag and the migration kinetics of doped boundaries is still lacking, especially in technologically-relevant alloys. Through theoretical analysis, mesoscale modeling, and machine learning studies, we investigate GB segregation and solute drag and establish design maps relating drag effects to relevant alloy and GB properties, i.e., the complete alloy design space. We find that solute drag is dominant in immiscible alloys with far-from-dilute compositions in agreement with experimental observations of GB segregation in metallic alloys. Our analysis reveals that solute–solute interactions within the GB and the degree of segregation asymmetry greatly influence solute drag values. In broad terms, our work provides future avenues to employ GB segregation to control boundary dynamics during materials processing or under service conditions.

1. Introduction

Nearly all structural materials are polycrystalline aggregates; they are composed of differently oriented crystalline grains that are internally joined at grain boundaries (GBs). Such interfaces play a critical role in controlling many engineering properties, including mechanical strength [1–4], embrittlement [5–7], and corrosion [8–10] and wear [11,12] resistance. Understanding GB physics is, therefore, a key aspect of materials discovery and design efforts.

Owing to their local atomic environments, which differ considerably from the bulk, GBs in polycrystalline alloys provide preferential segregation sites for alloying elements. In this context, GB solute segregation is not viewed as an undesired alloying effect, but rather a near-atomic scale strategy to tailor materials properties [13]. Indeed, the direct manipulation of GB's chemical states has been found to influence a host of materials properties and processes, such as cohesion and fracture resistance [13,14], transport [15,16], electrochemical response [17], electrical conductivity [18,19], and processability during advanced manufacturing techniques [20]. Of particular interest is the impact of GB chemistry on boundary dynamics, as it influences microstructure formation and evolution pathways during processing treatments or under operating environments. For example, GB segregation has been used to mitigate grain coarsening and thermally stabilize nanograined structures [21–28]. Another example deals with solid-state activated sintering in which GB segregation has been used to control coarsening and densification rates [29–31].

Solute segregation to GBs influences boundary migration in two main mechanisms. The first is thermodynamic in which solute segregation reduces the GB free energy and, thus, the driving force for boundary migration [32]. The second effect is kinetic, termed dynamic solute drag. Segregated elements remain within the GB and the boundary has to drag these solutes, creating a drag force P which is a function of the GB velocity $\mathcal{V}$ [33–35]. The characteristic GB solute drag–velocity curve [33,36] is shown in Fig. 1, where solute drag increases with velocity up to a peak point defined by $(\mathcal{V}_{max}, P_{max})$. The shaded region in Fig. 1 defines a drag regime where increasing the GB velocity requires overcoming this drag force. The region beyond the peak point in the drag–velocity curve defines the breakaway regime, where the GB escapes its solute atmosphere and migrates with its intrinsic velocity. Understanding the structure of solute drag–velocity curves, specifically the location of the peak point, has direct technological implications. For example, alloying with elements that shifts the peak point to the upper right side [see Fig. 1] of the solute drag–velocity plane will result in metallic alloys with sluggish boundary dynamics up to larger driving forces for GB migration.

* Corresponding author at: Department of Materials Science and Engineering, Lehigh University, Bethlehem, PA, 18015, USA.
E-mail address: fadi@lehigh.edu (F. Abdeljawad).

https://doi.org/10.1016/j.actamat.2024.120037
Received 5 January 2024; Received in revised form 22 May 2024; Accepted 23 May 2024
Available online 25 May 2024
1359-6454/© 2024 Acta Materialia Inc. Published by Elsevier Ltd. All rights are reserved, including those for text and data mining, AI training, and similar technologies.

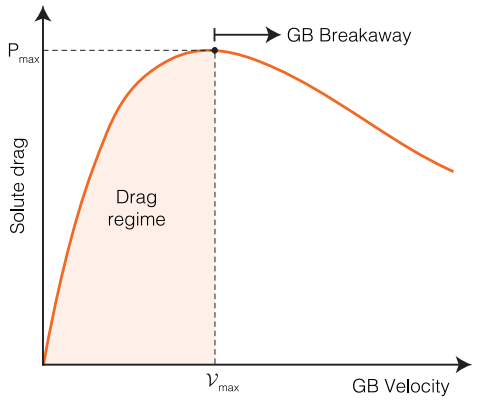

Fig. 1. A schematic of GB solute drag–velocity curve demonstrating drag and breakaway regimes. The peak point in solute drag is defined by (V_{max}, P_{max}).

GB solute segregation has been the subject of active research with a large body of work focused on the thermodynamics of GB segregation (i.e., reduction in GB energy with solute segregation) [32,37–42], the role of GB geometric degrees of freedom in boundary segregation [23,43–49], and segregation-induced GB transformations [50–56]. For example, Mishin [57] developed a discrete model of GB segregation and phase transformations to investigate the impact of GB phases on boundary mobility. Further, many experimental studies employing microscopy [23,24,26,58–65] and atom probe tomography [63,66–71] were used to examine GB composition profiles in a wide range of materials systems. More recently, data science and machine learning tools were employed to propose descriptors relating the local atomic environments to GB segregation energies [72–77]. While the aforementioned studies provide useful insights into GB segregation phenomena, GB solute drag effects (i.e., migration of doped GBs) remain unexplored. This is due to the fact that existing solute drag treatments employ several restrictive assumptions severely limiting their ability to quantify GB solute drag. For example, the solute drag treatment by Cahn [33] employed ideal and dilute alloys and more recent solute drag studies do not account for solute–solute interactions within GBs [35,78]. However, recent experimental studies revealed heavily doped GBs with solute concentration levels that are too high to be treated as ideal or dilute systems [21,23,25,79,80], and that such boundary concentrations can exceed the nominal bulk one by up to several orders of magnitude [13,81,82]. Indeed, recent studies highlighted the paramount role of non-ideality and solute–solute interactions in GB segregation energies [83–85]. A critical need, therefore, exists for a fundamental and quantitative understanding of the migration kinetics of doped GBs in concentrated alloy systems, especially as recent progress in alloy design has been geared towards systems with far-from-dilute compositions [86,87].

In addition to the aforementioned limitations, existing solute drag treatments consider symmetric GB segregation with respect to the boundary plane [33,35,88]. However, recent experimental studies demonstrated asymmetric and highly complex GB chemical profiles [89–93]. Lejček [90] revealed uneven solute distributions across GBs in a Fe–Si alloy, while Xie et al. [92] showed asymmetric solute segregation to tilt GBs in a Mg-based alloy. Luo et *al.* [93] demonstrated highly asymmetric GB segregation profiles across an asymmetric mixed GB in Ti-doped WC–Co. Very recently, high-resolution microscopy and atomistic simulations revealed complex and asymmetric step-by-step segregation of Ag in a symmetric tilt GB in Cu [94].

The above observations highlight several gaps in our understanding of GB solute drag and migration kinetics of doped GBs in engineering alloys. Some specific questions are relevant here: What is the impact of solute–solute interactions within the GB on solute drag? Does the asymmetry in GB segregation profiles influence solute drag? To what extent does GB solute drag depend on bulk alloy types and concentration levels? How do we quantify such effects?

To address the above-mentioned questions, we follow a line of investigation that differs from most recent studies that mainly focus on calculating site-specific GB segregation energies [72,73,76]. Using a recently developed mesoscale model [36], we perform theoretical analysis and computational and machine learning (ML) studies to explore GB solute drag in non-ideal, binary alloys and in GBs with various spatial profiles for their solute concentrations. The modeling framework accounts for solute–solute interactions in both the bulk alloy and GBs, and it captures asymmetric GB segregation. A key feature of our proposed modeling approach is its ability to capture GB solute drag and migration kinetics over diffusive scales that are not attainable with atomistic tools. The theoretical model reveals that solute drag is a sensitively dependent function of several materials parameters—solute drag is a hypersurface. Numerical solution of the resultant nonlinear governing equation is used to construct a dataset of GB solute drag–velocity profiles, which is then employed to train an artificial neural network model to predict the GB solute drag hypersurface. The ML model is used to scan the complete alloy and GB space to arrive at simple design rules relevant to GB segregation and migration kinetics of doped GBs.

2. Modeling framework

2.1. Theory

A schematic depicting our proposed theoretical treatment and mesoscale modeling of GB segregation and solute drag is shown in Fig. 2. The proposed mesoscale model is based on a recently published study by the authors [36]. First, we consider a semi-infinite bicrystal binary alloy of host element A and solute B described using a solute composition field $c(x,t)$, where x is the direction measured from the GB and t is time. Next, we employ regular solution thermodynamics for the functional form of the free energy of the bulk f_b and that of the GB f_{gb}, which are given by [36,95]

$$f_i = G_i^B c + G_i^A (1-c) + k_B T\left[c\ln(c) + (1-c)\ln(1-c)\right] + \Omega_i c(1-c), \quad i = gb, b, \tag{1}$$

where G^A and G^B describe the free energy of solvent A and solute B, respectively, k_B is Boltzmann constant, and T is temperature. Ω_b and Ω_{gb} are, respectively, the bulk and GB heat of mixing model parameters. The first two terms on the right-hand side of Eq. (1) correspond to the free energy of the alloy mixture, the third term describes configurational entropy, and the last term accounts for the heat of mixing of the solution. In regular solution thermodynamics, $\Omega \propto \epsilon_{AB} - 0.5(\epsilon_{AA} + \epsilon_{BB})$, where ϵ_{ij} is the i-j bond energy. With this convention, zero energy is the state where the atoms are separated to infinity and ϵ_{AA}, ϵ_{BB}, and ϵ_{AB} are negative quantities [95]. Further, positive Ω values describe repulsive A-B interactions, where regimes with $\Omega/(k_B\mathrm{T}) > 2$ result in phase separation [95], and negative values control the degree of mixing of the alloy. Our work treats both the bulk, Ω_b, and GB, Ω_{gb}, solute interactions as independent parameters, an assumption that was used in prior studies of GB segregation [38,96].

Next, at the mesoscale our model accounts for GB segregation profiles (e.g., symmetric, asymmetric) by introducing an indicator function $Y(x)$ that interpolates the energy between the bulk and GB such that the free energy at any point is given by $f = (1-Y)f_b + Y f_{gb}$. In the bulk grains $Y = 0$ and in the GB region Y peaks to a value of one with a prescribed spatial profile, thereby accounting for asymmetric segregation effects. Cahn's solute drag treatment [33] employed a symmetric triangle function that peaks at the center of the GB. In our recent work [36], we employed a Gaussian function instead, as it can also be used to locate the GB region, but it presents the advantage of

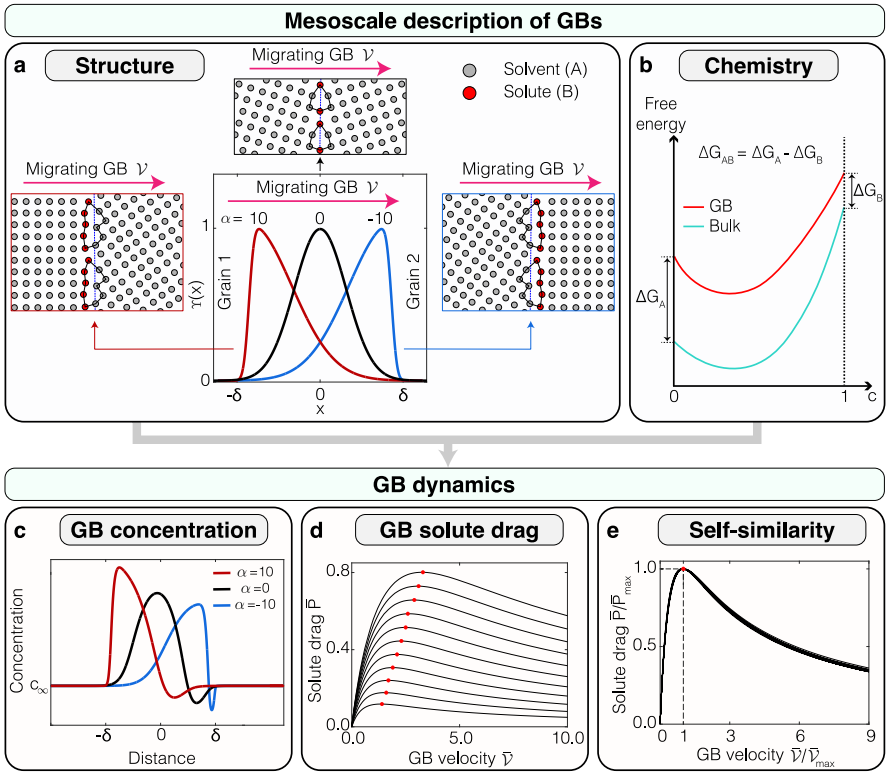

Fig. 2. Overview of our mesoscale model of GB segregation and solute drag. (a) The structure of the Y function, where the parameter α describes the degree of GB segregation asymmetry. Positive (negative) α values describe segregation to the trailing (leading) end of the migrating GB. $\alpha = 0$ corresponds to symmetric segregation. (b) Representative bulk and GB free energies demonstrating a graphical representation of $\Delta G_{AB} = \Delta G_A - \Delta G_B$. (c) Solute concentration profile across a migrating GB using $\alpha = -10, 0, 10$. (d) Representative GB solute drag–velocity curves showing a shift in the peak point. (e) Demonstration of self-similarity in solute drag, where the curves in (d) are re-scaled using solute drag $\bar{P}_{max}$ and GB velocity $\bar{\mathcal{V}}_{max}$ values at the peak point, resulting in collapse of the curves.

being a differentiable function. To allow for a systematic exploration of the impact of GB segregation asymmetry on solute drag, a natural extension of the Gaussian function is to use the skew-normal function for $Y(x)$ [Fig. 2(a)] given by [97]

$$Y(x) = Z\phi\left(\frac{x-\xi}{\omega}\right)\Phi\left(\frac{\alpha(x-\xi)}{\omega}\right), \tag{2}$$

where ϕ and Φ are the standard normal distribution and its cumulative density function, respectively, and $Z = 1/\max(\phi\Phi)$. ξ, ω, and α are parameters that control the mean, variance, and skewness of $Y(x)$, respectively. According to Fig. 2(a), $\alpha > 0$ results in positive skewness in which solutes occupy sites at the trailing end of the migrating GB, whereas negative skewness given by $\alpha < 0$ leads to solute segregation on the leading end of the GB. The case of $\alpha = 0$ corresponds to symmetric segregation, where Y reduces to the Gaussian function. Again, the use of $Y(x)$, shown in Fig. 2(a), to incorporate complex GB segregation profiles is motivated by recent high-resolution microscopy studies revealing asymmetric GB segregation in a wide range of alloys [92–94]. Here, we note that α is boundary specific, each GB in a given alloy microstructure could in principle have a distinct α value. In addition to using Eqs. (1) and (2) to interpolate the free energy between bulk and interfacial components, one can also add a contribution due to the transition region separating the bulk phase and GB regions [38].

Using the free energy description of the bulk and GB, the diffusion potential is given by

$$\mu = \mu_B - \mu_A = df/dc = df_b/dc - E, \tag{3}$$

where μ_A and μ_B are the chemical potentials of A and B, respectively, and

$$E = [\Delta G_{AB} + (2c-1)(\Omega_{gb} - \Omega_b)]Y \tag{4}$$

is the solute–GB interaction energy, which is concentration-dependent. Here, $\Delta G_{AB} = \Delta G_A - \Delta G_B$, where $\Delta G_A = (G^A_{gb} - G^A_b) = \gamma^A_{gb} v_m/2\delta$, $\Delta G_B = (G^B_{gb} - G^B_b) = \gamma^B_{gb} v_m/2\delta$, v_m is the atomic volume and 2δ is the GB layer width [98]. ΔG_A and ΔG_B represent the GB energy of pure A, γ^A_{gb}, and pure B, γ^B_{gb}, respectively, and ΔG_{AB}, therefore, describes the difference in GB energy between pure A (i.e., solvent) and that of pure B (i.e., solute). Fig. 2(b) shows schematics of GB and bulk free energy curves with a graphical representation of ΔG_A, ΔG_B, and ΔG_{AB}, where it can be seen that non-zero values for ΔG_{AB} result in titling of the GB free energy curve with respect to the bulk one.

The dependence of segregation energy E, Eq. (4), on the difference in GB energy of pure components brings an interesting point. Several studies [99–101] revealed that GB energy in a pure metal is correlated with the metal's shear modulus, which in the context of GB segregation suggests that positive values for $\Delta G_{AB} = \Delta G_A - \Delta G_B$ result from alloying a metal A with a softer (i.e., lower shear modulus) one B. Indeed, strong GB segregation was experimentally shown in systems, such as Fe–Zr [21,22], Pt–Au [23,24], W–Ti [25], Pd–Zr [27,28], in which the host metal was alloyed with a lower shear modulus solute.

Next, gradients in the chemical potential give rise to mass fluxes, and the steady state nonlinear solute transport equation expressed in a frame moving with the migrating GB at a constant velocity $\mathcal{V}$ is given by [see Appendix A for more details]

$$\frac{D_o Y}{k_B T} c(1-c)\frac{\partial \mu}{\partial x} = -\mathcal{V}\left(c - c_\infty\right), \tag{5}$$

where $D = D_o Y$ is the diffusion function, D_o is a reference GB diffusivity, and c_∞ is the far-field bulk concentration. It is shown in Appendix A that in the zero velocity limit, we recover an analytical solution of Eq. (5) in the form of segregation isotherms describing the GB concentration in terms of the alloy model parameters. This segregation isotherm corresponds to the Fowler–Guggenheim [96,102] model in regular solution alloys and to the McLean isotherm [103] in ideal solutions. Numerical solution of Eq. (5), detailed in Appendix A,

provides the concentration profile across the GB, see Fig. 2(c) for representative examples with various values for the α parameter, and this solute profile leads to a drag force P on the migrating GB given by [33]

$$P = -\frac{1}{v_m}\int_{-\infty}^{\infty}\left(c - c_\infty\right)\frac{dE}{dx}dx. \tag{6}$$

A close examination of Eq. (6) reveals that the spatial profile of the integrand $(c-c_\infty)dE/dx$ greatly influences the magnitude of solute drag P. This integrand is a function of several model parameters, including thermodynamic properties of the alloy (i.e., $\Omega_b, \Omega_{gb}, \Delta G_{AB}$), kinetics (i.e., $D_o, \mathcal{V}$), segregation asymmetry parameter α, overall alloy concentration c_∞, and temperature; the GB solute drag is a hypersurface. For example, if a particular choice of these model parameters results in even functions (i.e., symmetric with respect to the center of the GB region $x = 0$) for both the composition $c(x)$ and interaction energy $E(x)$, then the integrand $(c-c_\infty)dE/dx$ has an asymmetric profile with respect to $x = 0$ and the solute drag in this case is zero.

2.2. Non-dimensionalization

The governing equation for the solute concentration field, Eq. (5), and resultant solute drag P, Eq. (6), are expressed in non-dimensional form using the thermal energy of the alloy and GB half-width as reference energy and length scales, respectively, leading to the parameters: $\bar{\Omega}_b = \Omega_b/k_BT$, $\bar{\Omega}_{gb} = \Omega_{gb}/k_BT$, $\bar{x} = x/\delta$, $\Delta\bar{G}_{AB} = \Delta G_{AB}/k_BT$ and non-dimensional drag $\bar{P}$ and velocity $\bar{\mathcal{V}}$ given by

$$\bar{P} = Pv_m/k_BT \quad \text{and} \quad \bar{\mathcal{V}} = \mathcal{V}\delta/D_o. \tag{7}$$

Fig. 2(d) shows representative examples of GB drag–velocity curves for various values of materials parameters, where the peak points $(\bar{\mathcal{V}}_{max}, \bar{P}_{max})$ are shown in red markers. Very recently, Alkayyali and Abdeljawad [36] showed that GB solute drag–velocity curves exhibit a self-similar profile in which a characteristic solute drag curve G_{ref}, refer to Fig. 2(e), was obtained through re-scaling by the peak point values $(\bar{\mathcal{V}}_{max}, \bar{P}_{max})$. Such a re-scaling analysis indicates that one only needs knowledge about the peak point $(\bar{\mathcal{V}}_{max}, \bar{P}_{max})$ to fully characterize the GB solute drag–velocity curve, see Appendix A for more details on the characteristic drag–velocity curve.

2.3. Key model assumptions

Before we proceed with exploring the GB solute drag in the large alloy design space, it is important to highlight the key assumptions we made when deriving our modeling framework: (i) our model, by virtue of its construction, treats a GB as a region in space with a free energy function that is distinct from the bulk grains. (ii) Due to its mesoscale nature, our model does not capture site specific GB segregation; however, it is capable of treating segregation asymmetry using the function Y. (iii) We assume that the bulk alloy can be described by regular solution thermodynamics, where solute–solute interactions are accounted for using the heat of mixing parameter Ω. We do not consider alloys with large negative values for the heat of mixing parameter and associated ordering transitions, as most experimental studies of GB segregation have been found in alloys with some level of immiscibility [21–25,27,104]. (iv) Volume diffusion is frozen compared to the GB, an assumption valid in a wide range of alloys [105,106]. Further, in this work we do not consider the dependence of the diffusion coefficient across the boundary D_o on the GB geometry and concentration. It is straightforward, however, to include such dependencies if they are obtained from atomistic simulations [51,107,108]. (v) A close examination of Eq. (1) and the solute–GB interaction energy E reveals that the model parameter ΔG_{AB} describing the tilting of the GB and bulk free energy curves, see Fig. 2(b), yields a concentration-independent term to the segregation energy. In other words, ΔG_{AB} is the segregation energy in the limit of ideal or dilute alloys. Our model does not incorporate elasticity arising from the atomic size mismatch between host and solute atoms. This elastic contribution, however, can be incorporated in our treatment by augmenting the regular solution model parameter Ω with an elastic term that is a function of the alloy's elastic constants and dilatational strains due to atomic size mismatch [109]. (vi) The heat of mixing $\bar{\Omega}_{gb}$ and asymmetry α parameters are used to describe GB segregation, both of which can be obtained using atomistic simulations. For example, a study employing thermodynamic integration was used to calculate the GB free energy as a function of composition and temperature in a Cu–Ag alloy [41]. Other atomistic studies obtained site-specific segregation energies within the GB resulting in distributions for Ω_{gb} [83,110]. To enrich our modeling approach with such distributions, one can let the GB solute interaction parameter Ω_{gb} be spatially dependent to account for variations in segregation behavior within the GB region.

2.4. Artificial neural network model

The proposed mesoscale model reveals that solute drag $\bar{P}$ describing the migration of doped GBs is in general a nonlinear function of several bulk alloy and boundary properties and is written as

$$\bar{P} = \bar{P}(\Delta\bar{G}_{AB}, \bar{\Omega}_b, \bar{\Omega}_{gb}, c_\infty, \alpha). \tag{8}$$

Here, it is important to highlight the limitations of existing solute drag treatments which: (i) assume ideal systems without accounting for solute–solute interactions, $\bar{\Omega}_b = \bar{\Omega}_{gb} = 0$; (ii) only consider symmetric GB segregation, $\alpha = 0$; and (iii) target dilute alloys, $c_\infty < 0.001$. As a result, these treatments are only valid for a small subset of alloy and GB systems. Our work, on the other hand, relaxes these assumptions in order to quantitatively describe GB segregation and solute drag in a broad range of technologically-relevant alloy systems.

Eq. (5) provides the means to explore the solute drag hypersurface described by Eq. (8). To circumvent the computational cost associated with performing numerical simulations of the nonlinear solute drag governing equation, Eq. (5), under various input parameters, we propose an artificial neural network (ANN) model that is integrated with our physics-based mesoscale treatment. The ANN provides a low computational cost approach to quantifying the solute drag hypersurface across the complete alloy and GB space, and it leverages the self-similar nature of solute drag–velocity profiles to predict the peak point $(\bar{\mathcal{V}}_{max}, \bar{P}_{max})$ of these curves. The reader is referred to Appendix B for more details on ANN implementation, testing, and performance.

Fig. 3 depicts a schematic of the ANN architecture and analysis of its performance. The ANN is composed of an input-layer of materials parameters, one hidden-layer, and an output-layer, see Fig. 3(a). We employ our physics-based model to generate data for training and validating the proposed ANN, see Appendix B for details. Fig. 3(b) depicts a plot of R and MSE of the testing data as a function of the number of neurons in the hidden layer, where ANN underfitting (i.e., high MSE and low R values) can be seen when using a small number of neurons. Fig. 3(c)–(f) show quantification of the ANN MSE [Fig. 3(c) and (e)] and correlation between the predicted output and ground truth [Fig. 3(d) and (f)] for $\bar{P}_{max}$ [Fig. 3(c)–(d)] and $\bar{\mathcal{V}}_{max}$ [Fig. 3(e) and (f)], demonstrating excellent agreement between ANN predictions and ground truth data. As an additional validation step, we use model alloys with $(\bar{\Omega}_b, c_\infty, \Delta\bar{G}_{AB}) = (1.5, 1\%, 0)$ and generate a new set of ground truth data using new values for α and $\bar{\Omega}_{gb}$. Fig. 3(g) and (h) shows respectively ANN surface plots of $\bar{P}_{max}$ and $\bar{\mathcal{V}}_{max}$ as a function of the segregation asymmetry α and GB heat of mixing $\bar{\Omega}_{gb}$ parameters along with ground truth data in black markers. Again, excellent agreement between ANN predictions for $\bar{P}_{max}$ and $\bar{\mathcal{V}}_{max}$ and ground truth data can be observed.

The source code used to construct the ANN solute drag hypersurface is included in Supplementary Material, which enables interested readers to obtain solute drag values in the complete binary alloy space without the need to perform simulations of our GB segregation and solute drag model.

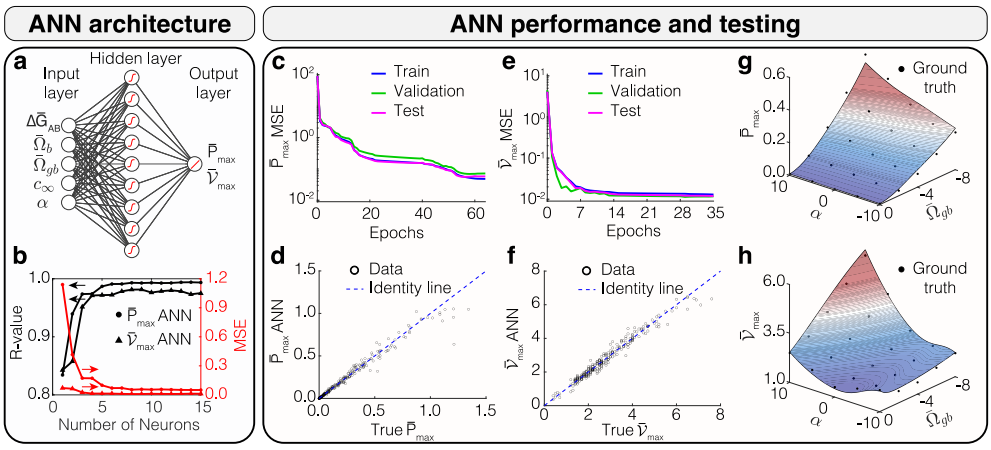

Fig. 3. Overview of the proposed ANN model. (a) The ANN architecture used to predict solute drag in the space parameterized by $\Delta\bar{G}_{AB}, \bar{\Omega}_b, \bar{\Omega}_{gb}, c_\infty$, and α. (b) A plot of the MSE and correlation coefficient, R, as a function of the number of neurons in the hidden layer. (c–f) ANN performance for (c–d) $\bar{P}_{max}$ and (e–f) $\bar{\mathcal{V}}_{max}$ depicting (e–e) MSE values; and (d–f) cross-validation, where ANN predictions are plotted against the ground truth data. The dashed lines correspond to the identity line. (g–h) For model alloys with ($\bar{\Omega}_b$, c_∞, $\Delta\bar{G}_{AB}$) = (1.5, 1%, 0), plots of the ANN surface and ground truth data (black markers) for (g) $\bar{P}_{max}$ and (h) $\bar{\mathcal{V}}_{max}$ as a function of α and $\bar{\Omega}_{gb}$.

3. Results and discussion

3.1. Learning the GB solute drag hypersurface

We now use the developed ANN model to scan the complete alloy and GB space in order to learn the general features of the GB solute drag hypersurface. Again, in this work the space describing metallic alloys and GB segregation character is parameterized by $\Delta\bar{G}_{AB}, \bar{\Omega}_b, \bar{\Omega}_{gb}, c_\infty$, and α. Graphically, $\Delta\bar{G}_{AB}$ describes the tilting of the GB free energy curve, which is related to the difference in GB energy between pure A, γ^A_{gb}, and that of pure B, γ^B_{gb}; c_∞ is the nominal alloy concentration; and α [see Fig. 2(a)] describes the degree of GB segregation asymmetry; and $\bar{\Omega}_b$ and $\bar{\Omega}_{gb}$ account for solute–solute interactions within the bulk and GB, respectively. In this work, the bulk $\bar{\Omega}_b$ and GB $\bar{\Omega}_{gb}$ heat of mixing model parameters are assumed to be independent, mainly due to GBs having atomic environments that differ considerably from the bulk. A recent study revealed spectral representations of GB heat of mixing interaction parameter based on site specific distributions of GB segregation energy [110]. Based on thermodynamic databases of metallic alloys, it was shown that the bulk and GB heat of mixing interaction parameters can take on a wide range of values [104,111,112]. Further, we consider cases with heat of mixing parameter $\bar{\Omega} < 2$, as alloys with $\bar{\Omega} > 2$ lead to phase separation. While we acknowledge that the interaction of moving GBs with precipitates is an interesting problem, this work mainly focuses on exploring the solute drag hypersurface.

Motivated by experimental observations [23–26] of strong GB segregation in immiscible bulk alloys with $\bar{\Omega}_b > 0$, we start by examining solute drag in a family of alloys with $\bar{\Omega}_b = 1.5$ as a function of $\Delta\bar{G}_{AB}, \bar{\Omega}_{gb}, c_\infty$, and α. We show cases with $\Delta\bar{G}_{AB} = 0$, 2, and 4, where Fig. 4(a1), (b1), and (c1) depicts schematics of the GB and bulk free energy curves with $\Delta\bar{G}_{AB} = 0, 2$, and 4, respectively. Fig. 4(a2), (b2), and (c2) shows contour slices of the maximum solute drag $\bar{P}_{max}$ and Fig. 4(a3), (b3), and (c3) shows the corresponding velocity $\bar{\mathcal{V}}_{max}$ at this maximum drag value for $\Delta\bar{G}_{AB}$ values of zero [Fig. 4(a2) and (a3)], two [Fig. 4(b2) and (b3)], and four [Fig. 4(c2) and (c3)]. The contour slices are plotted as a function of bulk concentration c_∞, GB heat of mixing $\bar{\Omega}_{gb}$, and GB segregation asymmetry α parameters. It can be seen that increasing $\Delta\bar{G}_{AB}$ leads to a large increase in solute drag [see Fig. 4(a2), (b2), and (c2)]. Recall that $\Delta\bar{G}_{AB} = (\gamma^A_{gb} - \gamma^B_{gb})v_m/2\delta k_B T$, which indicates that alloys with large solute drag values are ones with large differences in the GB energy between the host material and that of the solute.

Next, for immiscible bulk alloys with a given $\Delta\bar{G}_{AB}$ value, Fig. 4 shows larger GB segregation and solute drag $\bar{P}_{max}$ in miscible GBs that favor A-B mixing. Further, Fig. 4 reveals that asymmetric segregation with $\alpha > 0$, where solutes segregate to the trailing end of migrating GBs [see Fig. 2(a)], leads to larger drag than cases where solutes segregate to the leading end (i.e., $\alpha < 0$). This effect can be understood by examining Eq. (6), which predicts that solute drag arises due to the asymmetry in the integrand $(c - c_\infty)dE/dx$. A migrating GB with a velocity $\mathcal{V}$ will introduce asymmetric concentration profiles, see Fig. 2(c), thereby influencing the $(c - c_\infty)$ term in Eq. (6). In addition to this dynamic effect, asymmetry in segregation through the Y function will influence both the GB segregation energy E and concentration $(c - c_\infty)$ profiles in Eq. (6), and this asymmetric effect increases with α leading to larger solute drag values. A close examination of the contour slices in Fig. 4(a3), (b3), and (c3) reveals that the velocity $\bar{\mathcal{V}}_{max}$ at the peak point rapidly increases with increasing $\Delta\bar{G}_{AB}$ in GBs that are miscible (i.e., ones with $\bar{\Omega}_{gb} < 0$), where solutes prefer to segregate to the trailing end of the boundary (i.e., $\alpha > 0$). Such cases result in an increase in both $\bar{P}_{max}$ and $\bar{\mathcal{V}}_{max}$. Recall that increasing both $\bar{P}_{max}$ and $\bar{\mathcal{V}}_{max}$ shifts the peak point in the solute drag curve to the upper right side of the drag–velocity map [see Fig. 1] indicating sluggish GB dynamics up to larger velocities.

The contour slices in Fig. 4, which depicts GB solute drag in immiscible alloys with $\bar{\Omega}_b = 1.5$, reveal trends that have not been explored in prior studies of GB segregation, and it highlights the complex nature of the solute drag function in this high-dimensional alloy and GB space. For example, the slice of the solute drag hypersurface with $\Delta\bar{G}_{AB} = 4$ and asymmetry parameter $\alpha = 10$, which is enclosed by the dashed border line in Fig. 4(c2) and (c3), reveals multiple regimes with large drag values $\bar{P}_{max}$, but with considerable differences in their corresponding GB velocities $\bar{\mathcal{V}}_{max}$. This can be discerned by examining Fig. 5, which depicts surface plots of $\bar{P}_{max}$ and $\bar{\mathcal{V}}_{max}$ for this slice noting that it is now a function of GB heat of mixing parameter $\bar{\Omega}_{gb}$ and alloy composition c_∞ since $\bar{\Omega}_b = 1.5$, $\Delta\bar{G}_{AB} = 4$, and $\alpha = 10$. Fig. 5(a) reveals two local maxima in $\bar{P}_{max}$ corresponding to markedly different values for the GB heat of mixing parameter $\bar{\Omega}_{gb}$. The GB with $\bar{\Omega}_{gb} > 0$ exhibits larger solute drag compared to the one with $\bar{\Omega}_{gb} < 0$. However, Fig. 5(b) reveals large variations in the GB velocity $\bar{\mathcal{V}}_{max}$ at these two peak points. The velocity corresponding to the maximum solute drag with $\bar{\Omega}_{gb} = 1.95$ is much smaller than the case with $\bar{\Omega}_{gb} = -8$. Using the self-similar solute drag profile [see Appendix A] and the $\bar{\mathcal{V}}_{max}$ and $\bar{P}_{max}$ values at the points corresponding to the local maxima from Fig. 5(a) and (b), (c) shows solute drag–velocity curves for these points. It can be seen that while the peak solute drag values differ by ~35%, the GB velocity at these peak points varies by an order of magnitude. GB segregation with $\bar{\Omega}_{gb} < 0$ leads to solute drag regimes that extend to larger GB velocities.

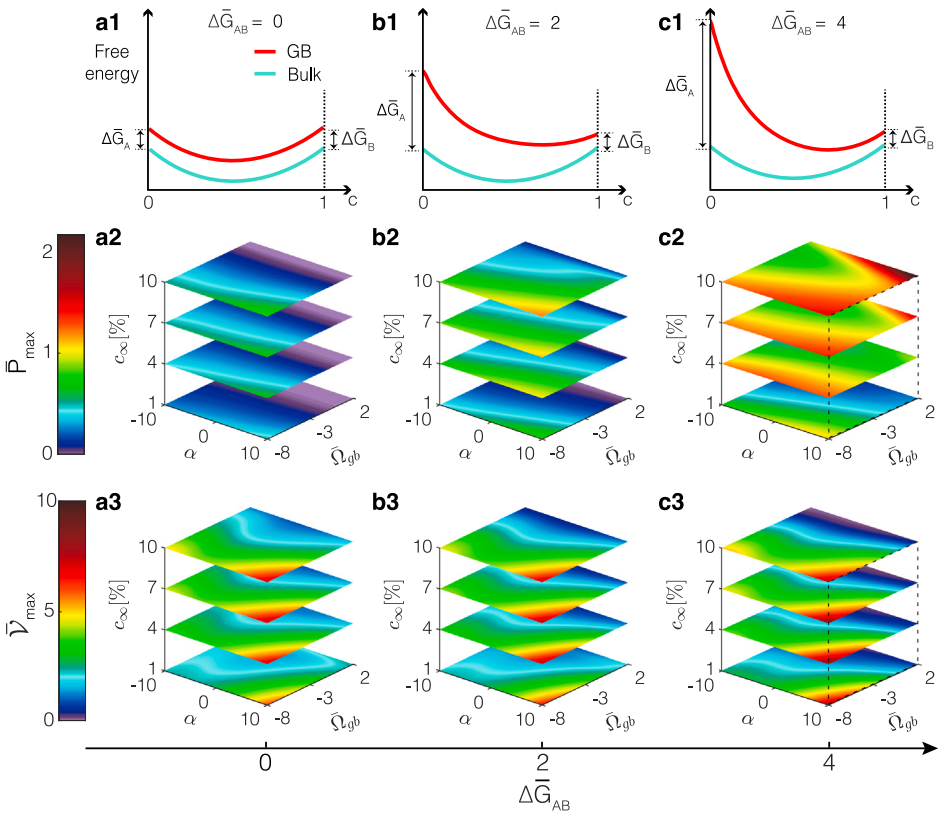

Fig. 4. Schematics of the bulk and GB free energy curves using: (a1) $\Delta\bar{G}_{AB} = 0$, (b1) $\Delta\bar{G}_{AB} = 2$, and (c1) $\Delta\bar{G}_{AB} = 4$. Using the ANN for an immiscible alloy with a bulk heat of mixing parameter $\bar{\Omega}_b = 1.5$, contour plots of (a2, b2, c2) $\bar{P}_{max}$ and (a3, b3, c3) $\bar{\mathcal{V}}_{max}$ on slice surfaces as a function of $\Delta\bar{G}_{AB}$ on the outside x-axis and the degree of segregation asymmetry α, GB heat of mixing $\bar{\Omega}_{gb}$, and bulk concentration c_∞ on the inside axes.

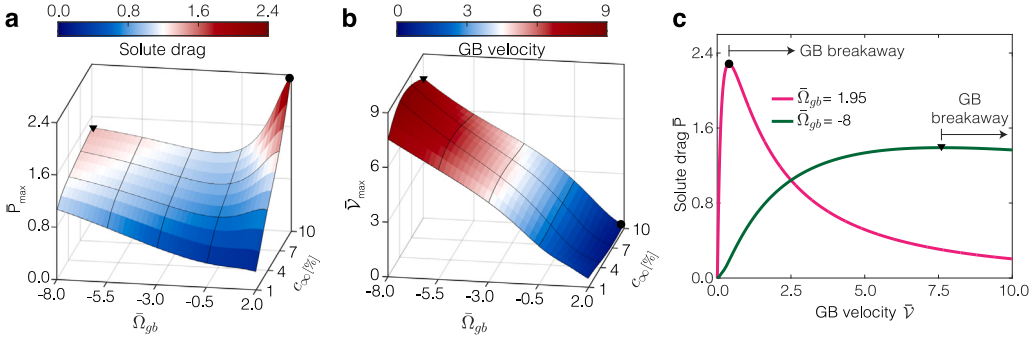

Fig. 5. For an immiscible bulk alloy with $\bar{\Omega}_b = 1.5$ and using GB parameters $(\Delta\bar{G}_{AB}, \alpha) = (4, 10)$, surface plots of (a) $\bar{P}_{max}$ and (b) $\bar{\mathcal{V}}_{max}$ for the contour slices in dashed black lines Fig. 4(c2) and (c3). (c) Using the self-similar solute drag profile and the peak point $(\bar{\mathcal{V}}_{max}, \bar{P}_{max})$, solute drag–velocity curves for the local maxima in panel (a), characterized by $(\bar{\Omega}_{gb}, c_\infty) = (1.95, 10\%)$ and $(-8, 10\%)$.

The observations in Figs. 4 and 5 for the GB solute drag hypersurface are for immiscible alloys, specifically ones with a bulk heat of mixing parameter $\bar{\Omega}_b = 1.5$. We now shift our attention to exploring the impact of bulk miscibility on solute drag in non-dilute alloys. To this end, we consider two families of alloys, ones with $\bar{\Omega}_b = -1.95$ favoring A-B mixing and immiscible systems with $\bar{\Omega}_b = 1.95$ indicating unfavorable A-B alloying. Fig. 6(a) through (c) shows contour slices of the maximum solute drag $\bar{P}_{max}$ as a function of the alloy concentration c_∞ and bulk heat of mixing parameter $\bar{\Omega}_b$ using the outside axes and as a function of the segregation asymmetry α, GB heat of mixing $\bar{\Omega}_{gb}$, and $\Delta\bar{G}_{AB}$ parameters using the inside axes. It can be seen that alloys with $\Omega_b > 0$ result in larger GB solute drag values compared to ones with $\Omega_b < 0$. Further, the increase in solute drag with α (i.e., segregation to the trailing end of the migrating GB) is more pronounced in immiscible alloys, this can be observed by comparing for example Fig. 6(c1) and (c2). It is also worth noting that increasing the alloy concentration c_∞ while fixing the other alloy parameters leads to an increase in solute drag. For example, for alloys with $(\Delta\bar{G}_{AB}, \alpha) = (2, 10)$, Fig. 6(d) shows a plot of solute drag as a function of c_∞ for various $\bar{\Omega}_{gb}$ values and for bulk alloys with $\bar{\Omega}_b$ of 1.95 and −1.95, where the nonlinear dependence of solute drag on bulk concentration can be observed. Further, for the model parameters used in Fig. 6(d), immiscible bulk alloys result in larger solute drag values compared to miscible systems. The observations from the surface slices in Figs. 4 and 6 reveal that GB solute drag increases with increasing $\Delta\bar{G}_{AB}$, $\bar{\Omega}_b$, c_∞, α, and decreasing $\bar{\Omega}_{gb}$.

3.2. The solute drag design map

We now develop a map of GB solute drag in the higher-dimensional alloy space, which can be used in alloy discovery efforts where the

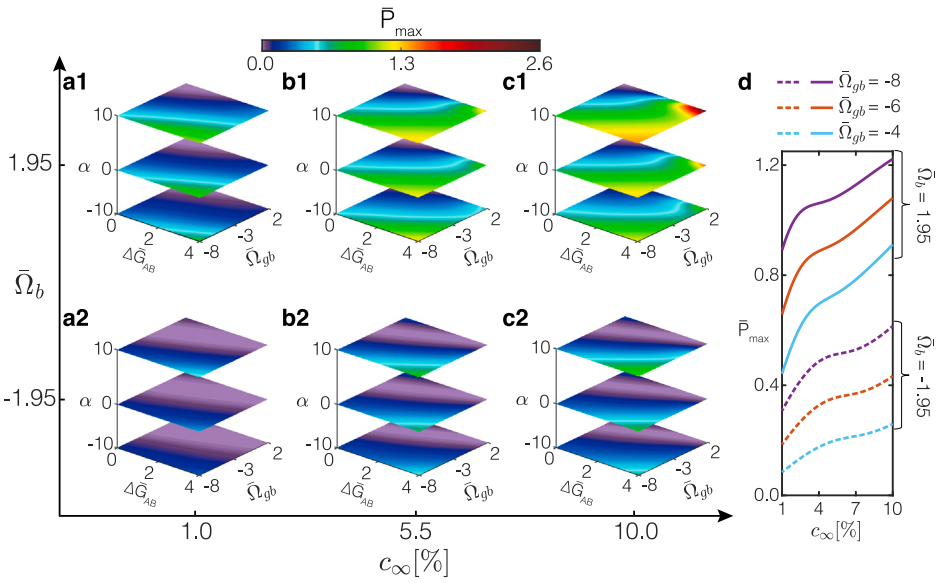

Fig. 6. The solute drag hypersurface. Using the outside axes, contour slices of solute drag for bulk compositions c_∞ of (a) 1%, (b) 5.5%, and (c) 10%, and for alloys with bulk heat of mixing $\bar{\Omega}_b$ values of (a1, b1, c1) 1.95 and (a2, b2, c2) −1.95. Using the inside axes, solute drag as a function of α, $\Delta\bar{G}_{AB}$, and $\bar{\Omega}_{gb}$. (d) For alloys with $(\Delta\bar{G}_{AB}, \alpha) = (2, 10)$, maximum solute drag as a function of bulk composition for alloys with $\bar{\Omega}_b = 1.95$ and −1.95 and GB heat of mixing $\bar{\Omega}_{gb} = -8, -6$, and -4. (For interpretation of the references to color in this figure legend, the reader is referred to the web version of this article.).

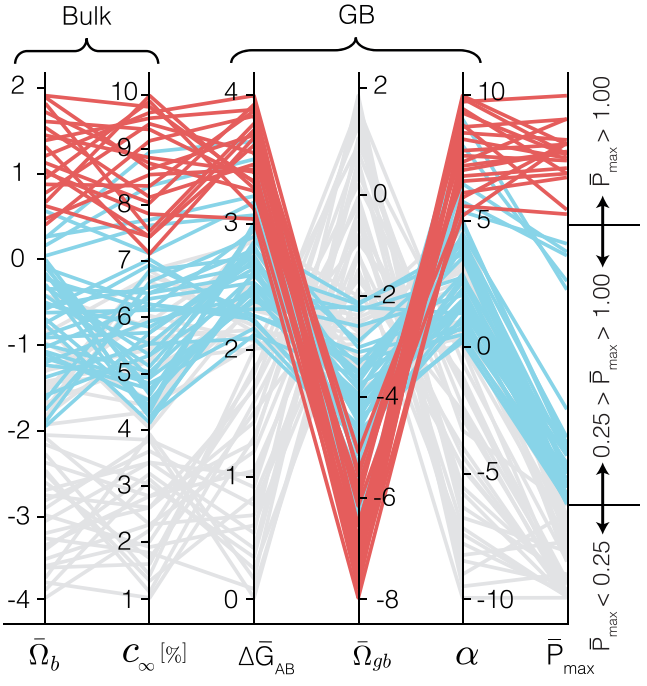

Fig. 7. GB solute drag design map. A parallel coordinate plot depicting maximum solute drag $\bar{P}_{max}$ as a function of bulk ($\bar{\Omega}_b$ and c_∞) and GB ($\Delta\bar{G}_{AB}$, $\bar{\Omega}_{gb}$, and α) parameters. We employ a three-tier color coding scheme of the solute drag curves, namely, red: $\bar{P}_{max} > 1.0$, cyan: $1.0 > \bar{P}_{max} > 0.25$, and gray: $\bar{P}_{max} < 0.25$. (For interpretation of the references to color in this figure legend, the reader is referred to the web version of this article.)

control of GB dynamics and optimization of grain microstructures are key design criteria. To this end, we use the ANN model to construct a parallel coordinate plot relating the maximum solute drag $\bar{P}_{max}$ to the model parameters $\bar{\Omega}_b, c_\infty, \Delta\bar{G}_{AB}, \bar{\Omega}_{gb}$, and α. Parallel coordinate plots allow for the analysis of the solute drag hypersurface, where every parameter is assigned an axis and all the axes are parallel to each other. Fig. 7 shows such a parallel axis plot, where the first two parallel axes are for $\bar{\Omega}_b$ and c_∞, which describe the bulk alloy; the third through fifth axes are for $\Delta\bar{G}_{AB}, \bar{\Omega}_{gb}$, and α, respectively, which describe the GB segregation character; and the last parallel axis is the solute drag one. As a result, each point in the solute drag hypersurface $\bar{P}(\Delta\bar{G}_{AB}, \bar{\Omega}_b, \bar{\Omega}_{gb}, c_\infty, \alpha)$ corresponds to a curve in Fig. 7.

As a demonstration of the potential use of Fig. 7 as an alloy design tool, we consider the case of GB segregation as a technique to mitigate grain coarsening in nanocrystalline alloys [40,104]. In this context, large solute drag leads to more thermally stable nanocrystalline materials with respect to grain coarsening. In addition to solute drag, GB segregation lowers the boundary energy, and thus the driving force for grain growth. We compare the solute drag values $\bar{P}_{max}$ to the driving force for curvature-driven grain coarsening $\bar{P}_{curv}$ given by [113–115]

$$\bar{P}_{curv} = \frac{v_m}{k_B T} \frac{2\gamma_{gb}}{L_{grain}}, \tag{9}$$

where γ_{gb} is the GB energy and L_{grain} is the grain size. The factor v_m/k_BT is introduced to make the driving force non-dimensional in the same way solute drag values are expressed in Fig. 7. Solute drag is effective in mitigating GB migration when $\bar{P}_{max} > \bar{P}_{curv}$. For our analysis, we use the following representative values: $\gamma_{gb} = 2$ J/m^2, an operating temperature of 500 K, $v_m \approx 9$ Å^3, and consider nanocrystalline alloys with $L_{grain} = 20$ nm. This results in $\bar{P}_{curv} \approx 0.25$.

We employ a three-tier color coding scheme of the solute drag curves in Fig. 7, namely, red: $\bar{P}_{max} > 1.0$, cyan: $1.0 > \bar{P}_{max} > 0.25$, and gray: $\bar{P}_{max} < 0.25$. Values of solute drag $\bar{P}_{max}$ less than 0.25 (i.e., gray curves in Fig. 7) are smaller than the driving force for grain coarsening $\bar{P}_{curv}$, which indicate that solute drag does not play a major role in hindering GB migration. Solute drag values between 0.25 and 1.0 are on the same order of magnitude as $\bar{P}_{curv}$, and, as a result, solute drag plays an important role in controlling GB dynamics. Cases where $\bar{P}_{max} > 1.0$ (i.e., red curves in Fig. 7) indicate that solute drag is much greater than $\bar{P}_{curv}$ and, therefore, it plays a dominant effect in hindering GB migration. Fig. 7 shows curves corresponding to representative points from the solute drag hypersurface, which reveal candidate alloys for applications where thermal stability with respect to grain coarsening is a key design criterion. Large solute drag values, compared with the driving force for grain growth in nanocrystalline alloys, are achieved in non-dilute and immiscible systems with $\Omega_b > 0$. For the GB parameters, regimes with large solute drag values are observed with $\Delta\bar{G}_{AB} > 0$

indicating alloys, where the pure host metal A is characterized by higher GB energies than those in the solute one B. Further, large solute drag values are observed in GBs with $\Omega_{gb} < 0$ and ones with asymmetric segregation, where solutes preferentially occupy sites on the trailing end of migrating GBs, i.e., $\alpha > 0$, according to our convention in Fig. 2(a). The strong impact of c_∞, Ω_b, and Ω_{gb} on solute drag can be also seen in Fig. 6(d) depicting $\bar{P}_{max}$ as a function of bulk composition c_∞ for various values of bulk Ω_b and GB Ω_{gb} heat of mixing parameters.

Next, we compare the solute drag predictions from our Fig. 7 to recent experimental studies of segregation-driven sluggish GB dynamics in metallic alloys. To this end, we choose Pt–Au, W–Ti, and Al–Mg alloys as many studies revealed strong GB segregation and thermal stability with respect to GB migration and grain coarsening in these systems [23–26]. To place these alloys on our solute drag map, we obtain the bulk regular solution parameter of these alloys from existing thermodynamic databases [116–118] at conditions similar to the published experimental studies [24–26], the reader is referred to Appendix C for more details on how to obtain bulk regular solution model parameters for these alloys. For the Pt-10 at.% Au at 700 °C [24], $\bar{\Omega}_b = 2.75$ [116], while the W-20 at.% Ti at 1100 °C [25], $\bar{\Omega}_b = 1.8$ [117]. The Al-5 at.% Mg at 300 °C [26] has $\bar{\Omega}_b = 0.22$ [118]. Therefore, the data for these (Pt–Au, W–Ti, Al–Mg) alloys with non-dilute solute concentrations of (10 at.%, 20 at.%, 5 at.%) and bulk regular solution interaction parameters of (2.75, 1.8, 0.22) place them on the upper ends of the bulk heat of mixing $\bar{\Omega}_b$ and alloy concentration c_∞ axes in Fig. 7. This in turn suggests large GB solute drag in these alloys, which contributes to their experimentally observed stability with respect to grain coarsening.

While Fig. 7 presents trends from our model in the complete alloy space, we recognize that the comparison of our model predictions to these experimentally observed, thermally stable alloys (i.e., Pt–Au, W–Ti, and Al–Mg) is limited. This is mainly due to the lack of experimental data probing the segregation asymmetry and GB heat of mixing, which correspond to the third through fifth parallel axes in Fig. 7. However, atomistic simulations can be used to calculate solute interactions within the GB, enabling a quantification of the GB heat of mixing parameter Ω_{gb}. For example, a study by Frolov and Mishin [41] employed thermodynamic integration in conjunction with the Gibbs adsorption equation to calculate the GB free energy as a function of composition in a Cu–Ag alloy. Recent studies obtained site-specific segregation energies within the GB leading to a spectral representation of Ω_{gb} [83,110]. Further, atomistic simulations or high-resolution microscopy can be used to construct an order parameter mapping out the chemical profile across the GB region, an approach that was used in studies of other materials interfaces [119]. Such an approach allows for a quantification of the segregation asymmetry parameter α. Another future work will be to extend our model to account for two- or three-dimensional GB geometries, thus allowing for the incorporation of spatially dependent GB parameters, such as Ω_{gb} or α. Finally, our solute drag model can be extended to account for disconnection-mediated GB motion by both incorporating recently developed frameworks for GB disconnection energetics [120,121] and accounting for solute-disconnection interactions.

4. Summary and conclusion

In summary, we examined in this work GB segregation and dynamic solute drag; a phenomenon that plays a critical role during materials processing treatments or under operating environments. Existing solute drag treatments consider dilute alloys without accounting for solute–solute interactions in the boundary region. Further, these models only capture symmetric segregation, however, recent advances in microscopy techniques revealed asymmetric segregation in several boundary geometries. These shortcomings render existing solute drag models unpredictive, especially in advanced alloy systems with far-from-dilute compositions. Our work addresses these gaps by developing a mesoscale GB solute drag model and employing ANN techniques to efficiently explore solute drag in the large alloy and GB parameter space. The resulting physics-based nonlinear governing equation from our model was numerically solved to generate datasets to train and validate an ANN. We established a solute drag design map demarcating solute drag regimes across the complete alloy and GB space. It was found that alloys with unfavorable A-B mixing, i.e., $\bar{\Omega}_b > 0$, and non-dilute concentrations increase solute drag considerably compared to ideal (i.e., $\bar{\Omega}_b = 0$) systems. Further, asymmetric GB segregation, where solutes pile up on the trailing end of the migrating boundary, results in larger solute drag values compared to cases with symmetric segregation. Finally, the difference in GB energy between the pure host metal and pure solute one was shown to increase the GB segregation energy, and, thus, solute drag. In broader terms, our proposed work provides robust alloy design maps that can be used to engineer advanced metallic alloys with controlled GB segregation levels and boundary dynamics.

CRediT authorship contribution statement

Malek Alkayyali: Writing – review & editing, Writing – original draft, Visualization, Methodology, Investigation, Formal analysis, Data curation. **Milad Taghizadeh:** Writing – review & editing, Writing – original draft, Investigation, Formal analysis. **Fadi Abdeljawad:** Writing – review & editing, Writing – original draft, Supervision, Resources, Project administration, Methodology, Funding acquisition, Conceptualization.

Declaration of competing interest

The authors declare that they have no known competing financial interests or personal relationships that could have appeared to influence the work reported in this paper.

Acknowledgments

This work was supported by the U.S. Army Research Office through the Young Investigator Program [award: W911NF-20-2-0122] and the National Science Foundation (NSF), United States [DMR 2114832].

Appendix A. Mathematical model

Model derivation

Given the proposed energy functional in Eq. (1), the diffusion potential is given by

$$\mu = G_b^B - G_b^A + k_B T \ln\left(\frac{c}{1-c}\right) + \Omega_b(1-2c) - \left[\Delta G_{AB} + (2c-1)(\Omega_{gb} - \Omega_b)\right] Y. \tag{A.1}$$

Gradients in the chemical potential result in a mass flux J given by

$$J = -\frac{Dc(1-c)}{k_B T}\nabla\mu, \tag{A.2}$$

where D is the solute diffusion function normal to the migrating GB, assumed to be $D(x) = D_o Y(x)$ and D_o is a reference GB diffusivity. Using a frame of reference moving with the GB at a velocity $\mathcal{V}$, the non-dimensional steady-state mass transport governing equation is

$$\frac{\partial}{\partial \bar{x}}\left[Yc(1-c)\frac{\partial \bar{\mu}}{\partial \bar{x}}\right] + \bar{\mathcal{V}}\frac{\partial c}{\partial \bar{x}} = 0, \tag{A.3}$$

where $\bar{x} = x/\delta$, $\bar{\mu} = \mu/k_B T$, and $\bar{\mathcal{V}} = \mathcal{V}\delta/D_o$. Eq. (A.3) is integrated using the far-field boundary condition $c \to c_\infty$ as $\bar{x} \to -\infty$, which gives

$$Yc(1-c)\frac{\partial \bar{\mu}}{\partial \bar{x}} = -\bar{\mathcal{V}}\left(c - c_\infty\right). \tag{A.4}$$

With the aid of the diffusion potential function in Eq. (A.1), we obtain the following governing equation in terms of the solute concentration field c

$$\frac{dc}{d\bar{x}} = \frac{g_1 c^3 + g_2 c^2 + g_3 c + \bar{\mathcal{V}} c_\infty}{g_4\left(c^2 - c\right) + g_5}, \tag{A.5}$$

where

$$\begin{aligned} g_1 &= -2(\bar{\Omega}_{gb} - \bar{\Omega}_b) Y \frac{dY}{d\bar{x}}, \\ g_2 &= \left(3(\bar{\Omega}_{gb} - \bar{\Omega}_b) - \Delta\bar{G}_{AB}\right) Y \frac{dY}{d\bar{x}}, \\ g_3 &= \left(\Delta\bar{G}_{AB} - \bar{\Omega}_{gb} + \bar{\Omega}_b\right) Y \frac{dY}{d\bar{x}} - \bar{\mathcal{V}}, \\ g_4 &= 2Y\left[\bar{\Omega}_{gb} Y + \bar{\Omega}_b (1 - Y)\right], \\ g_5 &= Y. \end{aligned} \tag{A.6}$$

Here, $\Delta\bar{G}_{AB} = \Delta G_{AB}/k_B T$, $\bar{\Omega}_b = \Omega_b/k_B T$, and $\bar{\Omega}_{gb} = \Omega_{gb}/k_B T$. Once the solute concentration field is obtained through the numerical solution of Eq. (A.5), GB solute drag is evaluated using Eq. (6).

Equilibrium behavior: Segregation isotherm

For a stationary GB at equilibrium (i.e., $\bar{\mathcal{V}} = 0$), Eq. (A.3) becomes

$$Y c(1 - c) \frac{\partial \bar{\mu}}{\partial \bar{x}} = 0, \tag{A.7}$$

where the non-dimensional chemical potential $\bar{\mu} = \mu/k_B T$ is obtained using Eq. (A.1). Integrating Eq. (A.7) once and using the far-field boundary condition $c \to c_\infty$ as $\bar{x} \to -\infty$, we get the following transcendental solution

$$\frac{c}{1 - c} = \frac{c_\infty}{1 - c_\infty} \exp\left[2\bar{\Omega}_b\left(c - c_\infty\right) + \left(\Delta\bar{G}_{AB} - \left(\bar{\Omega}_{gb} - \bar{\Omega}_b\right)(1 - 2c)\right) Y\right], \tag{A.8}$$

which represents the segregation isotherm.

Mesoscale simulations

The governing equation for GB segregation and solute drag, Eq. (A.5), was solved numerically with several GB velocities $\bar{\mathcal{V}}$ using a second-order modified Rosenbrock scheme suitable for stiff differential equations [122,123]. GB solute drag–velocity curves are constructed using Eq. (6) by performing the integration numerically using the trapezoidal rule. Recently, we revealed that solute drag curves exhibit a self-similar behavior with a characteristic curve $G_{\text{ref}}\left(\bar{\mathcal{V}}/\bar{\mathcal{V}}_{max}\right)$ of the form [36]

$$\begin{aligned} \frac{\bar{P}}{\bar{P}_{max}} &= G_{\text{ref}}\left(\bar{\mathcal{V}}/\bar{\mathcal{V}}_{max}\right) \\ &= \frac{1}{\left(\frac{\bar{\mathcal{V}}}{\bar{\mathcal{V}}_{max}}\right)} \exp\left[\frac{4.62 - \left(\ln\left(\frac{\bar{\mathcal{V}}}{\bar{\mathcal{V}}_{max}}\right) - 2.15\right)^2}{4.3}\right], \quad \frac{\bar{\mathcal{V}}}{\bar{\mathcal{V}}_{max}} > 0 \end{aligned} \tag{A.9}$$

Appendix B. Training the artificial neural network

To develop our ANN model of GB solute drag, we simulated Eq. (A.5) using 1500 parameter sets in the five-dimensional design space, i.e., $\Delta\bar{G}_{AB}$, $\bar{\Omega}_b$, $\bar{\Omega}_{gb}$, c_∞, and α, where Latin hypercube [124–127] is used for sampling. Of the 1500 parameter sets that were simulated using our physics-based model, 1000 samples were used as a training dataset to train the ANN and 500 were used to validate and test the performance of the ANN. The 500 samples were split into a validation dataset, which was used to prevent overfitting, and a testing dataset to measure the overall performance of the trained ANN. For each one of these parameter sets, the drag–velocity curve is generated by numerically solving Eqs. (5) and (6) using velocities in the range of 0 to 100 with an increment of 0.1. Then, solute drag–velocity curves were constructed using Eq. (6), and the maximum point $(\bar{\mathcal{V}}_{max}, \bar{P}_{max})$ of the drag curves were obtained and used to train and validate the ANN.

In this work, we used a shallow ANN to predict the peak point $(\bar{\mathcal{V}}_{max}, \bar{P}_{max})$ of solute drag curves as shown in Fig. 3(a). The ANN consists of an input-layer with five inputs (i.e., $\Delta\bar{G}_{AB}$, $\bar{\Omega}_b$, $\bar{\Omega}_{gb}$, c_∞, α), one hidden-layer with neurons employing the standard logistic transfer function, and an output-layer employing a linear function. To optimize the number of neurons in the hidden layer, we trained the ANN using one to fifteen neurons and recorded the correlation coefficient (R) and the mean squared error (MSE) for the testing dataset. Fig. 3(b) depicts a plot of R-value and MSE as a function of the number of neurons, where ANN underfitting (i.e., high MSE and low R values) can be seen when using a small number of neurons. As the number of neurons increases, the ANN performance improves until it reaches a plateau when the number of neurons exceeds nine, which is what we used for all results reported in this work.

In Fig. 3(c) and (e), we record the MSE of training, validation, and testing datasets as a function of the epoch number. In ANN training, an *epoch* refers to a complete training iteration where the entire training dataset was used to adjust the ANN parameters (i.e., weights and biases) [128]. In this work, we quantified the ANN performance using the MSE of two different ground truth datasets, validation and testing, after completing each epoch. Tracking the validation MSE serves as a means for preventing overfitting and early stopping once the validation MSE starts to increase during training [129,130]. The testing MSE provides another layer of measuring the ANN performance using a ground truth dataset that has not been used in training the ANN.

Appendix C. Calculations of bulk regular solution parameters

Published phase diagram data were used to obtain bulk chemical free energies of Pt–Au [116], W–Ti [117], and Al–Mg [118] alloys. Representative bulk compositions and temperatures of the ones used experimentally were employed, namely Pt–10 at.% Au at 700 °C [24], W–20 at.% Ti at 1100 °C [25], and Al–5 at.% Mg at 300 °C [26]. Under these conditions, Pt–Au alloy has a regular solution parameter Ω_b = 22.3 kJ/mol [116] corresponding to $\bar{\Omega}_b$ = 2.75; W–Ti has Ω_b = 20.6 kJ/mol [117] leading to $\bar{\Omega}_b$ = 1.8; and Ω_b = 1.1 kJ/mol is for Al–Mg [118] corresponding to $\bar{\Omega}_b$ = 0.22.

Appendix D. Supplementary data

A Matlab code of the ANN solute drag hypersurface is provided using the link below. For a metallic alloy with given $\Delta\bar{G}_{AB}, \bar{\Omega}_b, \bar{\Omega}_{gb}, c_\infty$, and α parameters, the code provides the values of peak solute drag and corresponding velocity.

Supplementary material related to this article can be found online at https://doi.org/10.1016/j.actamat.2024.120037.

References

[1] E.O. Hall, The deformation and ageing of mild steel: III discussion of results, Proc. Phys. Soc. B 64 (1951) 747–753.

[2] N.J. Petch, The cleavage strength of polycrystals, J. Iron Steel 174 (1953) 25–28.

[3] J. Wyrzykowski, M. Grabski, The hall–petch relation in aluminium and its dependence on the grain boundary structure, Phil. Mag. A 53 (1986) 505–520.

[4] F. Sansoz, J. Molinari, Mechanical behavior of σ tilt grain boundaries in nanoscale Cu and Al: A quasicontinuum study, Acta Mater. 53 (2005) 1931–1944.

[5] R. Messmer, C. Briant, The role of chemical bonding in grain boundary embrittlement, Acta Metall. 30 (1982) 457–467.

[6] S.P. Lynch, Mechanisms and kinetics of environmentally assisted cracking: current status, issues, and suggestions for further work, Metall. Mater. Trans. A 44 (2013) 1209–1229.

[7] P. Lejček, M. Šob, V. Paidar, Interfacial segregation and grain boundary embrittlement: An overview and critical assessment of experimental data and calculated results, Prog. Mater. Sci. 87 (2017) 83–139.

[8] L. Beaunier, Corrosion of grain boundaries: initiation processes and testing, J. Phys. Colloq. 43 (1982) C6–271.

[9] K. Ralston, N. Birbilis, C. Davies, Revealing the relationship between grain size and corrosion rate of metals, Scr. Mater. 63 (2010) 1201–1204.

[10] A. Joshi, D.F. Stein, Chemistry of grain boundaries and its relation to intergranular corrosion of austenitic stainless steel, Corrosion 28 (1972) 321–330.

[11] J.F. Curry, T.F. Babuska, T.A. Furnish, P. Lu, D.P. Adams, A.B. Kustas, B.L. Nation, M.T. Dugger, M. Chandross, B.G. Clark, et al., Achieving ultralow wear with stable nanocrystalline metals, Adv. Mater. 30 (2018) 1802026.

[12] W. Zhai, L. Bai, R. Zhou, X. Fan, G. Kang, Y. Liu, K. Zhou, Recent progress on wear-resistant materials: designs, properties, and applications, Adv. Sci. 8 (2021) 2003739.

[13] D. Raabe, M. Herbig, S. Sandlöbes, Y. Li, D. Tytko, M. Kuzmina, D. Ponge, P.-P. Choi, Grain boundary segregation engineering in metallic alloys: A pathway to the design of interfaces, Curr. Opin. Solid State Mater. Sci. 18 (2014) 253–261.

[14] M. Seah, Interface adsorption, embrittlement and fracture in metallurgy: A review, Surf. Sci. 53 (1975) 168–212.

[15] C. Herzig, S.V. Divinski, Grain boundary diffusion in metals: recent developments, Mater. Trans. 44 (2003) 14–27.

[16] M.R. Soares, C.A. Costa, E.M. Lanzoni, J. Bettini, C.A. Ramirez, F.L. Souza, E. Longo, E.R. Leite, Unraveling the role of sn segregation in the electronic transport of polycrystalline hematite: raising the electronic conductivity by lowering the grain-boundary blocking effect, Adv. Electron. Mater. 5 (2019) 1900065.

[17] M.J. Duarte, J. Klemm, S.O. Klemm, K.J.J. Mayrhofer, M. Stratmann, S. Borodin, A.H. Romero, M. Madinehei, D. Crespo, J. Serrano, et al., Element-resolved corrosion analysis of stainless-type glass-forming steels, Science 341 (2013) 372–376.

[18] D. Mattissen, D. Raabe, F. Heringhaus, Experimental investigation and modeling of the influence of microstructure on the resistive conductivity of a Cu–Ag–Nb in situ composite, Acta Mater. 47 (1999) 1627–1634.

[19] D. Raabe, S. Ohsaki, K. Hono, Mechanical alloying and amorphization in Cu–Nb–Ag in situ composite wires studied by transmission electron microscopy and atom probe tomography, Acta Mater. 57 (2009) 5254–5263.

[20] Z. Sun, X. Tan, C. Wang, M. Descoins, D. Mangelinck, S.B. Tor, E.A. Jägle, S. Zaefferer, D. Raabe, Reducing hot tearing by grain boundary segregation engineering in additive manufacturing: example of an alxcocrfeni high-entropy alloy, Acta Mater. 204 (2021) 116505.

[21] K. Darling, B. VanLeeuwen, C. Koch, R. Scattergood, Thermal stability of nanocrystalline Fe–Zr alloys, Mater. Sci. Eng. A 527 (2010) 3572–3580.

[22] K. Darling, B. VanLeeuwen, J. Semones, C. Koch, R. Scattergood, L. Kecskes, S. Mathaudhu, Stabilized nanocrystalline iron-based alloys: Guiding efforts in alloy selection, Mater. Sci. Eng. A 528 (2011) 4365–4371.

[23] C.M. Barr, S.M. Foiles, M. Alkayyali, Y. Mahmood, P.M. Price, D.P. Adams, B.L. Boyce, F. Abdeljawad, K. Hattar, The role of grain boundary character in solute segregation and thermal stability of nanocrystalline Pt–Au, Nanoscale 13 (2021) 3552–3563.

[24] P. Lu, F. Abdeljawad, M. Rodriguez, M. Chandross, D. Adams, B. Boyce, B. Clark, N. Argibay, On the thermal stability and grain boundary segregation in nanocrystalline ptau alloys, Materialia 6 (2019) 100298.

[25] T. Chookajorn, C.A. Schuh, Nanoscale segregation behavior and high-temperature stability of nanocrystalline w–20 at.% ti, Acta Mater. 73 (2014) 128–138.

[26] A. Devaraj, W. Wang, R. Vemuri, L. Kovarik, X. Jiang, M. Bowden, J. Trelewicz, S. Mathaudhu, A. Rohatgi, Grain boundary segregation and intermetallic precipitation in coarsening resistant nanocrystalline aluminum alloys, Acta Mater. 165 (2019) 698–708.

[27] C. Krill III, H. Ehrhardt, R. Birringer, Thermodynamic stabilization of nanocrystallinity, Int. J. Mater. Res. 96 (2005) 1134–1141.

[28] B.K. VanLeeuwen, K.A. Darling, C.C. Koch, R.O. Scattergood, B.G. Butler, Thermal stability of nanocrystalline Pd81Zr19, Acta Mater. 58 (2010) 4292–4297.

[29] H. Hayden, J. Brophy, The activated sintering of tungsten with group viii elements, J. Electrochem. Soc. 110 (1963) 805.

[30] K. Hwang, H. Huang, Identification of the segregation layer and its effects on the activated sintering and ductility of Ni-doped molybdenum, Acta Mater. 51 (2003) 3915–3926.

[31] M. Park, C.A. Schuh, Accelerated sintering in phase-separating nanostructured alloys, Nature Commun. 6 (2015) 6858.

[32] J. Weissmüller, Alloy effects in nanostructures, Nanostruct. Mater. 3 (1993) 261–272.

[33] J.W. Cahn, The impurity-drag effect in grain boundary motion, Acta Metall. 10 (1962) 789–798.

[34] K. Lücke, H. Stüwe, On the theory of impurity controlled grain boundary motion, Acta Metall. 19 (1971) 1087–1099.

[35] M. Mendelev, D. Srolovitz, A regular solution model for impurity drag on a migrating grain boundary, Acta Mater. 49 (2001) 589–597.

[36] M. Alkayyali, F. Abdeljawad, Grain boundary solute drag model in regular solution alloys, Phys. Rev. Lett. 127 (2021) 175503.

[37] J. Weissmüller, W. Krauss, T. Haubold, R. Birringer, H. Gleiter, Atomic structure and thermal stability of nanostructured Y–Fe alloys, Nanostruct. Mater. 1 (1992) 439–447.

[38] J.R. Trelewicz, C.A. Schuh, Grain boundary segregation and thermodynamically stable binary nanocrystalline alloys, Phys. Rev. B 79 (2009) 094112.

[39] R. Kirchheim, Reducing grain boundary, dislocation line and vacancy formation energies by solute segregation. I. Theoretical background, Acta Mater. 55 (2007) 5129–5138.

[40] R. Kirchheim, Grain coarsening inhibited by solute segregation, Acta Mater. 50 (2002) 413–419.

[41] T. Frolov, Y. Mishin, Thermodynamics of coherent interfaces under mechanical stresses. II. Application to atomistic simulation of grain boundaries, Phys. Rev. B 85 (2012) 224107.

[42] P. Lejček, S. Hofmann, Thermodynamics of grain boundary segregation and applications to anisotropy, compensation effect and prediction, Crit. Rev. Solid State Mater. Sci. 33 (2008) 133–163.

[43] A. Gupta, X. Zhou, G.B. Thompson, G.J. Tucker, Role of grain boundary character and its evolution on interfacial solute segregation behavior in nanocrystalline Ni–P, Acta Mater. 190 (2020) 113–123.

[44] B. Powell, D. Woodruff, Anisotropy in grain boundary segregation in copper-bismuth alloys, Philos. Mag. 34 (1976) 169–176.

[45] P. Lejček, J. Adámek, S. Hofmann, Anisotropy of grain boundary segregation in $\sigma = 5$ bicrystals of α-iron, Surf. Sci. 264 (1992) 449–454.

[46] P. Wynblatt, D. Chatain, Anisotropy of segregation at grain boundaries and surfaces, Metall. Mater. Trans. A 37 (2006) 2595–2620.

[47] A. Seki, D. Seidman, Y. Oh, S. Foiles, Monte carlo simulations of segregation at [001] twist boundaries in a Pt (Au) alloy—I. Results, Acta Metall. Mater. 39 (1991) 3167–3177.

[48] J. Rittner, D. Seidman, Solute-atom segregation to ⟨110⟩ symmetric tilt grain boundaries, Acta Mater. 45 (1997) 3191–3202.

[49] D.N. Seidman, Subnanoscale studies of segregation at grain boundaries: Simulations and experiments, Annu. Rev. Mater. Res. 32 (2002) 235–269.

[50] D. Raabe, S. Sandlöbes, J. Millán, D. Ponge, H. Assadi, M. Herbig, P.-P. Choi, Segregation engineering enables nanoscale martensite to austenite phase transformation at grain boundaries: a pathway to ductile martensite, Acta Mater. 61 (2013) 6132–6152.

[51] T. Frolov, S. Divinski, M. Asta, Y. Mishin, Effect of interface phase transformations on diffusion and segregation in high-angle grain boundaries, Phys. Rev. Lett. 110 (2013) 255502.

[52] T. Futazuka, R. Ishikawa, N. Shibata, Y. Ikuhara, Grain boundary structural transformation induced by co-segregation of aliovalent dopants, Nat. Commun. 13 (2022) 5299.

[53] Y. Yan, M. Chisholm, G. Duscher, A. Maiti, S. Pennycook, S. Pantelides, Impurity-induced structural transformation of a mgo grain boundary, Phys. Rev. Lett. 81 (1998) 3675.

[54] J. Brown, Y. Mishin, Segregation and structural transformations at $\sigma = 3$ grain boundaries in NiAl: A Monte-Carlo study, Acta Mater. 53 (2005) 2149–2156.

[55] C. O'Brien, C. Barr, P. Price, K. Hattar, S. Foiles, Grain boundary phase transformations in ptau and relevance to thermal stabilization of bulk nanocrystalline metals, J. Mater. Sci. 53 (2018) 2911–2927.

[56] N. Zhou, C. Hu, J. Luo, Grain boundary segregation transitions and critical phenomena in binary regular solutions: A systematics of complexion diagrams with universal characters, Acta Mater. 221 (2021) 117375.

[57] Y. Mishin, Solute drag and dynamic phase transformations in moving grain boundaries, Acta Mater. 179 (2019) 383–395.

[58] Z. Yu, P.R. Cantwell, Q. Gao, D. Yin, Y. Zhang, N. Zhou, G.S. Rohrer, M. Widom, J. Luo, M.P. Harmer, Segregation-induced ordered superstructures at general grain boundaries in a nickel-bismuth alloy, Science 358 (2017) 97–101.

[59] B. Krakauer, D. Seidman, Systematic procedures for atom-probe field-ion microscopy studies of grain boundary segregation, Rev. Sci. Instrum. 63 (1992) 4071–4079.

[60] W. Kingery, J. Vander Sande, T. Mitamura, Scanning transmission electron microscopy investigation of grain-boundary segregation in a ZnO–bi/sub 2/o/sub 3/varistor, J. Am. Ceram. Soc. (US) 62 (1979).

[61] V. Keast, D. Williams, Quantification of boundary segregation in the analytical electron microscope, J. Microsc. 199 (2000) 45–55.

[62] S.C. Pun, W. Wang, A. Khalajhedayati, J.D. Schuler, J.R. Trelewicz, T.J. Rupert, Nanocrystalline Al–Mg with extreme strength due to grain boundary doping, Mater. Sci. Eng. A 696 (2017) 400–406.

[63] M. Herbig, D. Raabe, Y. Li, P. Choi, S. Zaefferer, S. Goto, Atomic-scale quantification of grain boundary segregation in nanocrystalline material, Phys. Rev. Lett. 112 (2014) 126103.

[64] Z. Peng, T. Meiners, Y. Lu, C.H. Liebscher, A. Kostka, D. Raabe, B. Gault, Quantitative analysis of grain boundary diffusion, segregation and precipitation at a sub-nanometer scale, Acta Mater. 225 (2022) 117522.

[65] A. Stoffers, O. Cojocaru-Mirédin, W. Seifert, S. Zaefferer, S. Riepe, D. Raabe, Grain boundary segregation in multicrystalline silicon: correlative characterization by ebsd, ebic, and atom probe tomography, Prog. Photovolt., Res. Appl. 23 (2015) 1742–1753.

[66] O.C. Hellman, D.N. Seidman, Measurement of the Gibbsian interfacial excess of solute at an interface of arbitrary geometry using three-dimensional atom probe microscopy, Mater. Sci. Eng. A 327 (2002) 24–28.
[67] L. Li, Z. Li, A.K. da Silva, Z. Peng, H. Zhao, B. Gault, D. Raabe, Segregation-driven grain boundary spinodal decomposition as a pathway for phase nucleation in a high-entropy alloy, Acta Mater. 178 (2019) 1–9.
[68] K. Babinsky, J. Weidow, W. Knabl, A. Lorich, H. Leitner, S. Primig, Atom probe study of grain boundary segregation in technically pure molybdenum, Mater. Charact. 87 (2014) 95–103.
[69] A.S. Ebner, S. Jakob, H. Clemens, R. Pippan, V. Maier-Kiener, S. He, W. Ecker, D. Scheiber, V.I. Razumovskiy, Grain boundary segregation in Ni-base alloys: A combined atom probe tomography and first principles study, Acta Mater. 221 (2021) 117354.
[70] A.J. Detor, M.K. Miller, C.A. Schuh, Measuring grain-boundary segregation in nanocrystalline alloys: direct validation of statistical techniques using atom probe tomography, Philos. Mag. Lett. 87 (2007) 581–587.
[71] S.-I. Baik, M. Olszta, S. Bruemmer, D.N. Seidman, Grain-boundary structure and segregation behavior in a nickel-base stainless alloy, Scr. Mater. 66 (2012) 809–812.
[72] L. Huber, R. Hadian, B. Grabowski, J. Neugebauer, A machine learning approach to model solute grain boundary segregation, NPJ Comput. Mater. 4 (2018) 1–8.
[73] M. Wagih, P.M. Larsen, C.A. Schuh, Learning grain boundary segregation energy spectra in polycrystals, Nat. Commun. 11 (2020) 1–9.
[74] M. Wagih, C.A. Schuh, Learning grain-boundary segregation: From first principles to polycrystals, Phys. Rev. Lett. 129 (2022) 046102.
[75] J. Messina, R. Luo, K. Xu, G. Lu, H. Deng, M.A. Tschopp, F. Gao, Machine learning to predict aluminum segregation to magnesium grain boundaries, Scr. Mater. 204 (2021) 114150.
[76] Y. Mahmood, M. Alghalayini, E. Martinez, C.J. Paredis, F. Abdeljawad, Atomistic and machine learning studies of solute segregation in metastable grain boundaries, Sci. Rep. 12 (2022) 1–12.
[77] C. Hu, J. Luo, Data-driven prediction of grain boundary segregation and disordering in high-entropy alloys in a 5d space, Mater. Horiz. (2022).
[78] K. Lücke, G. Gottstein, Grain boundary motion–I. Theory of vacancy production and vacancy drag during grain boundary motion, Acta Metall. 29 (1981) 779–789.
[79] A.J. Detor, C.A. Schuh, Tailoring and patterning the grain size of nanocrystalline alloys, Acta Mater. 55 (2007) 371–379.
[80] A.K. Da Silva, D. Ponge, Z. Peng, G. Inden, Y. Lu, A. Breen, B. Gault, D. Raabe, Phase nucleation through confined spinodal fluctuations at crystal defects evidenced in Fe–Mn alloys, Nat. Commun. 9 (2018) 1–11.
[81] S. Hofmann, Segregation at grain boundaries, Surf. Segreg. Phenom. (1990) 107–134.
[82] S. Hofmann, P. Leiĉek, Solute segregation at grain boundaries, Interface Sci. 3 (1996) 241–267.
[83] T.P. Matson, C.A. Schuh, Atomistic assessment of solute-solute interactions during grain boundary segregation, Nanomaterials 11 (2021) 2360.
[84] M. Wagih, C.A. Schuh, Grain boundary segregation beyond the dilute limit: Separating the two contributions of site spectrality and solute interactions, Acta Mater. 199 (2020) 63–72.
[85] D. Scheiber, L. Romaner, R. Pippan, P. Puschnig, Impact of solute-solute interactions on grain boundary segregation and cohesion in molybdenum, Phys. Rev. Mater. 2 (2018) 093609.
[86] Y. Zhang, T.T. Zuo, Z. Tang, M.C. Gao, K.A. Dahmen, P.K. Liaw, Z.P. Lu, Microstructures and properties of high-entropy alloys, Prog. Mater. Sci. 61 (2014) 1–93.
[87] E.P. George, D. Raabe, R.O. Ritchie, High-entropy alloys, Nat. Rev. Mater. 4 (2019) 515–534.
[88] M. Hillert, B. Sundman, A treatment of the solute drag on moving grain boundaries and phase interfaces in binary alloys, Acta Metall. 24 (1976) 731–743.
[89] S. Dregia, P. Wynblatt, C. Bauer, Summary abstract: The segregation of gold at copper/silver interphase boundaries, J. Vacuum Sci. Technol. A 5 (1987) 1746–1747.
[90] P. Lejček, Characterization of grain boundary segregation in an Fe–Si alloy, Anal. Chim. Acta 297 (1994) 165–178.
[91] P. Lejček, S. Hofmann, Thermodynamics and structural aspects of grain boundary segregation, Crit. Rev. Solid State Mater. Sci. 20 (1995) 1–85.
[92] H. Xie, Q. Huang, J. Bai, S. Li, Y. Liu, J. Feng, Y. Yang, H. Pan, H. Li, Y. Ren, et al., Nonsymmetrical segregation of solutes in periodic misfit dislocations separated tilt grain boundaries, Nano Lett. 21 (2021) 2870–2875.
[93] Z. Luo, C. Hu, L. Xie, H. Nie, C. Xiang, X. Gu, J. He, W. Zhang, Z. Yu, J. Luo, A highly asymmetric interfacial superstructure in wc: Expanding the classic grain boundary segregation and new complexion theories, Mater. Horiz. 7 (2020) 173–180.
[94] L. Langenohl, T. Brink, G. Richter, G. Dehm, C.H. Liebscher, Atomic-resolution observations of silver segregation in a [111] tilt grain boundary in copper, Phys. Rev. B 107 (2023) 134112.
[95] D. Porter, K. Easterling, Phase Transformations in Metals and Alloys, CRC Press, 2009.
[96] P. Lejček, Grain Boundary Segregation in Metals, Springer, 2010.
[97] A. Azzalini, The Skew-Normal and Related Families, Vol. 3, Cambridge University Press, 2013.
[98] M. Hillert, Phase Equilibria, Phase Diagrams and Phase Transformations: Their Thermodynamic Basis, Cambridge University Press, 2007.
[99] D.L. Olmsted, S.M. Foiles, E.A. Holm, Survey of computed grain boundary properties in face-centered cubic metals: I. Grain boundary energy, Acta Mater. 57 (2009) 3694–3703.
[100] S.M. Foiles, Temperature dependence of grain boundary free energy and elastic constants, Scr. Mater. 62 (2010) 231–234.
[101] E.A. Holm, D.L. Olmsted, S.M. Foiles, Comparing grain boundary energies in face-centered cubic metals: Al, Au, Cu and Ni, Scr. Mater. 63 (2010) 905–908.
[102] R. Fowler, E. Guggenheim, Statistical Thermodynamics, Cambridge University Press, 1939.
[103] A.P. Sutton, R.W. Balluffi, Interfaces in Crystalline Materials, Clarendon Press, 1996.
[104] H.A. Murdoch, C.A. Schuh, Stability of binary nanocrystalline alloys against grain growth and phase separation, Acta Mater. 61 (2013) 2121–2132.
[105] J.C. Fisher, Calculation of diffusion penetration curves for surface and grain boundary diffusion, J. Appl. Phys. 22 (1951) 74–77.
[106] Y.R. Kolobov, G. Grabovetskaya, M. Ivanov, A. Zhilyaev, R. Valiev, Grain boundary diffusion characteristics of nanostructured nickel, Scr. Mater. 44 (2001) 873–878.
[107] Y. Mishin, C. Herzig, Grain boundary diffusion: recent progress and future research, Mater. Sci. Eng. A 260 (1999) 55–71.
[108] R. Koju, Y. Mishin, Atomistic study of grain-boundary segregation and grain-boundary diffusion in Al–Mg alloys, Acta Mater. 201 (2020) 596–603.
[109] T.W. Heo, S. Bhattacharyya, L.-Q. Chen, A phase field study of strain energy effects on solute–grain boundary interactions, Acta Mater. 59 (2011) 7800–7815.
[110] T.P. Matson, C.A. Schuh, Phase and defect diagrams based on spectral grain boundary segregation: A regular solution approach, Acta Mater. 265 (2024) 119584.
[111] H.A. Murdoch, C.A. Schuh, Estimation of grain boundary segregation enthalpy and its role in stable nanocrystalline alloy design, J. Mater. Res. 28 (2013) 2154–2163.
[112] T. Chookajorn, H.A. Murdoch, C.A. Schuh, Design of stable nanocrystalline alloys, Science 337 (2012) 951–954.
[113] J. Burke, D. Turnbull, Recrystallization and grain growth, Prog. Metal Phys. 3 (1952) 220–292.
[114] W.W. Mullins, Two-dimensional motion of idealized grain boundaries, J. Appl. Phys. 27 (1956) 900–904.
[115] G. Gottstein, L.S. Shvindlerman, Grain Boundary Migration in Metals: Thermodynamics, Kinetics, Applications, CRC Press, 2009.
[116] H. Okamoto, T. Massalski, The Au–Pt (gold-platinum) system, Bull. Alloy Phase Diag. 6 (1985) 46–56.
[117] J. Murray, The ti-w (titanium-tungsten) system, Bull. Alloy Phase Diag. 2 (1981) 192–196.
[118] J.L. Murray, The Al-Mg (aluminum- magnesium) system, J. Phase Equilib. 3 (1982) 60–74.
[119] K.-A. Wu, A. Karma, J.J. Hoyt, M. Asta, Ginzburg–Landau theory of crystalline anisotropy for bcc-liquid interfaces, Phys. Rev. B 73 (2006) 094101.
[120] L. Zhang, J. Han, Y. Xiang, D.J. Srolovitz, Equation of motion for a grain boundary, Phys. Rev. Lett. 119 (2017) 246101.
[121] J. Han, D.J. Srolovitz, M. Salvalaglio, Disconnection-mediated migration of interfaces in microstructures: I. Continuum model, Acta Mater. 227 (2022) 117178.
[122] T. Steihaug, A. Wolfbrandt, An attempt to avoid exact jacobian and nonlinear equations in the numerical solution of stiff differential equations, Math. Comp. 33 (1979) 521–534.
[123] L.F. Shampine, M.W. Reichelt, The matlab ode suite, SIAM J. Sci. Comput. 18 (1997) 1–22.
[124] M. Stein, Large sample properties of simulations using latin hypercube sampling, Technometrics 29 (1987) 143–151.
[125] A.B. Owen, Orthogonal arrays for computer experiments, integration and visualization, Stat. Sin. (1992) 439–452.
[126] W.-L. Loh, On latin hypercube sampling, Ann. Statist. 24 (1996) 2058–2080.
[127] M.D. McKay, R.J. Beckman, W.J. Conover, A comparison of three methods for selecting values of input variables in the analysis of output from a computer code, Technometrics 42 (2000) 55–61.
[128] J. Zupan, Introduction to artificial neural network (ann) methods: what they are and how to use them, J. Acta Chim. Slov. 41 (1994) 327–327.
[129] L. Prechelt, Early stopping-but when? in: Neural Networks: Tricks of the Trade, Springer, 1998, pp. 55–69.
[130] M.H. Beale, M.T. Hagan, H.B. Demuth, Neural network toolbox user's guide, MathWorks (2010) 77–81.